Letter

Phase diagram of twisted bilayer $MoTe_2$ in a magnetic field with an account for the electron-electron interaction

Minxuan Wang,[1,2] Xiaoyu Wang,[1] and Oskar Vafek[1,3]
[1]National High Magnetic Field Laboratory, Tallahassee, Florida 32310, USA
[2]Department of Physics, University of California, Berkeley, California 94720, USA
[3]Department of Physics, Florida State University, Tallahassee, Florida 32306, USA

(Received 25 June 2024; revised 21 October 2024; accepted 22 October 2024; published 15 November 2024)

We study electron-electron interaction-induced states of twisted bilayer $MoTe_2$ in an out-of-plane magnetic field $B\hat{\mathbf{z}}$ near one hole per moiré unit cell filling. The three-dimensional phase diagram showing the evolution of competing phases with B, interaction strength, and an out-of-plane electric field is presented at electron fillings that follow the Diophantine equation along the Chern number $-\mathrm{sgn}(B)$ line, that is pointing away from the charge neutral filling, where we find prominent Chern insulators consistent with the experiments. We also explain the experimental absence of prominent Chern insulators along the Chern number $+\mathrm{sgn}(B)$ line.

DOI: 10.1103/PhysRevB.110.L201107

Introduction. Moiré materials are well known for their tunability and hosting various correlated phases due to their narrow energy electronic bands [1,2]. Among these materials, twisted transition metal dichalcogenide (TMD) homobilayers, as well as heterobilayers, are predicted [3,4], and experimentally shown, to exhibit an integer quantum anomalous Hall (QAH) effect [5,6]. Intriguingly, a fractional quantum anomalous Hall effect has recently also been observed in twisted $MoTe_2$ homobilayer ($tMoTe_2$) [7–10], with a number of theoretical papers devoted to these integer and fractional Chern insulators [11–27]. Due to the large unit cell area A_{uc} of moiré materials, the out-of-plane magnetic field $B\hat{\mathbf{z}}$ has proven to be a powerful probe of their correlated states [7,8,28,29]. Particularly interesting is the evolution of such states in the ν-B plane, where the electron filling $\nu = \rho_e A_{\mathrm{uc}}$ and ρ_e is the areal density of electrons. The key tool is the thermodynamic formula [30,31] which states that the quantized Hall conductivity of a gapped state of electrons (with charge $-e$) at $T = 0$ follows

$$\sigma_{xy} = -\sigma_{yx} = -e\frac{\partial \rho_e}{\partial B}\bigg|_{\mu,T} = -t\frac{e^2}{h}. \tag{1}$$

Here, t is the Chern number [32] and we use SI units throughout. The Diophantine equation for ν is [33–37]

$$\nu = s + t\frac{\phi}{\phi_0}, \tag{2}$$

where the flux quantum $\phi_0 = h/e = 4136\ \mathrm{T\,nm^2}$ and the flux through the unit cell is $\phi = BA_{\mathrm{uc}}$.

A ubiquitous experimental observation in $tMoTe_2$ at twist angles in the 3.4°–3.9° range is the QAH state at $\nu = -1 = s$ evolving into a Chern state at $B \neq 0$ with a prominent gap at $t = -\mathrm{sgn}(B)$ and a noted absence of a prominent gap at $t = +\mathrm{sgn}(B)$ [7–10]. In other words, the Streda lines emanating from $\nu = -1$ point *away* from the charge neutrality point (CNP) for either sign of B. The two QAH states with opposite Chern numbers at $B = 0$ are partners under the time reversal symmetry, which is spontaneously broken, and therefore they must be equally stable at $B = 0$. The relative instability of the $t = +\mathrm{sgn}(B)$ state at $B \neq 0$ has thus far not been explained. Note that in 1.23° twisted WSe_2 bilayer the prominent Chern insulator line at $s = -1$ points *towards* the CNP [29], and that *both* behaviors have been observed in the magic angle twisted bilayer graphene device of Ref. [38], as well as in calculations [39].

Here, we show that, within our $B \neq 0$ self-consistent Hartree-Fock calculation at the twist angle 3.89° and the dielectric constant ϵ entering the interaction (4) chosen to reproduce the $B = 0$ QAH state [23], the ground state at $s = -1$ and $t = -\mathrm{sgn}(B)$ is valley polarized and that the holes preferentially populate the valley whose spin is aligned to the direction of the magnetic field. This state can be thought of as a Landau quantized QAH state with a nonvanishing (large) gap in the $B \to 0$ limit and we refer to it as a Chern paraelectric because it preserves $C_{2y}\mathcal{T}$, the combination of an in-plane twofold rotation symmetry and the time reversal symmetry. Its energy spectrum as a function of ϕ/ϕ_0 is shown in Fig. 1(a). Since the spin orientation of the holes in the two valleys is opposite due to the spin-valley locking [40], the valley polarization reverses upon reversing the sign of B [still at $t = -\mathrm{sgn}(B)$]. Interestingly, the nature of the lowest-energy state at $s = -1$ and $t = +\mathrm{sgn}(B)$ depends sensitively on g, the strength of the spin and orbital Zeeman coupling [41]. At $g = 0$, it is valley polarized but now the holes populate the valley whose spin is antialigned to the direction of the magnetic field. For a given B, it can be thought of as a Landau quantized time reversed partner of the QAH discussed above. Its (large) gap also does not vanish in the $B \to 0$ limit [see Fig. 1(d)]. If it were stable, the valley polarization would reverse at a fixed B upon changing the filling from $-1 - \frac{|\phi|}{\phi_0}$ to $-1 + \frac{|\phi|}{\phi_0}$, similar to the observations reported in Ref. [42] in graphene heterostructures. Such a state would appear as a prominent Chern insulator, inconsistent with the experiments [7–10]. At $g \gtrsim 2$, however, the ground state changes and the holes populate the valley with spin aligned to the direction of the magnetic field for a range of B that expands to lower

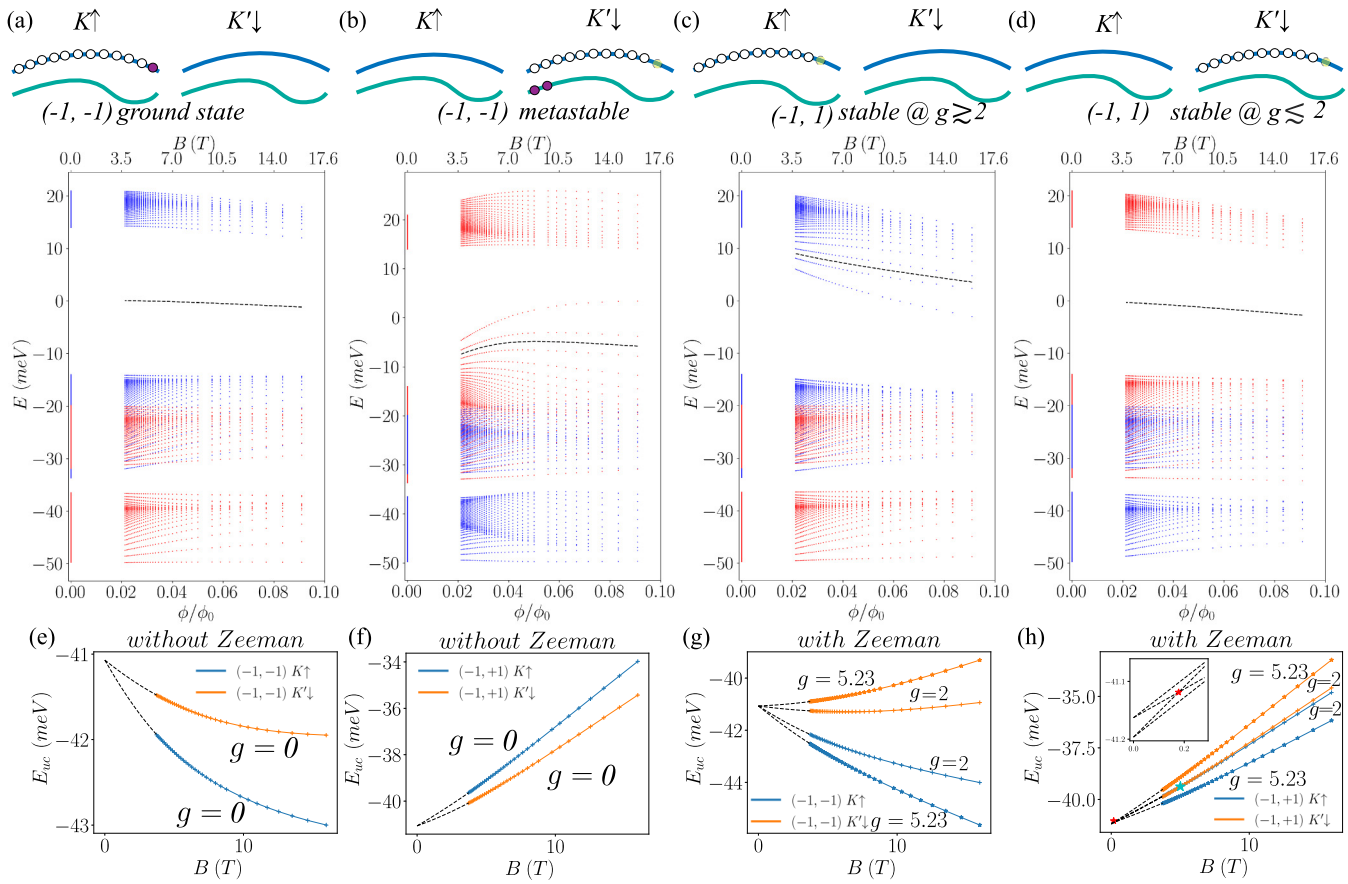

FIG. 1. (a)–(d) Hartree-Fock energy spectrum with varying magnetic field at $\nu = -1 - \frac{|\phi|}{\phi_0}$ and $\nu = -1 + \frac{|\phi|}{\phi_0}$. Electrons occupy all eigenstates below the black dashed line (guide to the eye). Blue (red) points represent eigenstates in the **K** (**K**′) valley. (e), (f) Total energy per unit cell vs magnetic field. Dashed lines are obtained from quadratic interpolation using calculated energy per unit cell at $B = 0$. (g), (h) Energy per unit cell with nonzero g factor.

$|B|$ as g increases [Fig. 1(h)]. It can be thought of as an integer quantum Hall (IQH) state, populating the lowest pair of Landau levels (LLs) of the Chern paraelectric excitation spectrum at $t = -\mathrm{sgn}(B)$ with electrons, as seen in Fig. 1(c). Because of the sizable band mass, its gap is small and vanishing as $B \to 0$, consistent with the experimental absence of a prominent Chern insulator at $t = +\mathrm{sgn}(B)$ and presence at $t = -\mathrm{sgn}(B)$. As detailed below, we estimate the orbital Zeeman contribution to g in $tMoTe_2$ to be 3.23 and of the same sign as the spin contribution 2, placing us safely in the $g \gtrsim 2$ regime. We note that the sophisticated *ab initio* calculation [43] yields a total Landé g factor $g = 9.17$, exceeding our estimate and placing the system deeper into the $g \gtrsim 2$ regime.

The perpendicular electric field D has also proved to be a powerful tool to probe and manipulate the nature of correlated states in $tMoTe_2$ [7–10]. In the experiments at $B = 0$, the spin-polarized QAH state transitions into a trivial insulator above a critical D_* [7–10]. The proximate trivial state is argued to be spin, and therefore valley, unpolarized in Ref. [8] and spin, and therefore valley, polarized in Ref. [10]. Such a topological transition is also seen in the Hartree-Fock calculation at $B = 0$ [23,27], and the spin structure of the trivial state depends on the value of ϵ. For $\epsilon > \epsilon' \approx 19$ the transition is directly into a spin-unpolarized intervalley coherent state (IVC) and for $\epsilon_* \approx 15.4 < \epsilon < \epsilon'$ the proximate trivial state is valley polarized (VP). This can be seen in the $B = 0$ plane of Fig. 2 where we vary the D-induced potential difference between two layers u_D. Intriguingly, at $B \neq 0$ and $t = -\mathrm{sgn}(B)$ a sharp change of compressibility can be seen in the experiment at the same D_* as the transition at $B = 0$ (see extended data

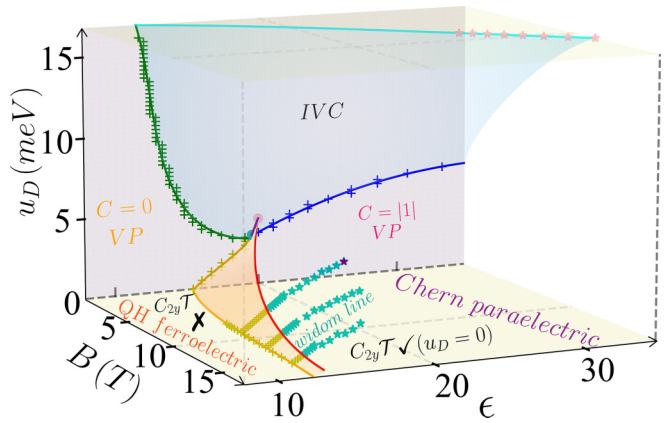

FIG. 2. Tentative phase diagram of $tMoTe_2$ at $\nu = -1 - \frac{|\phi|}{\phi_0}$ and 3.89° twist. The blue surface at $B \neq 0$ denotes the boundary between the IVC state and two valley $U(1)$ preserving states, Chern paraelectric and QH ferroelectric.

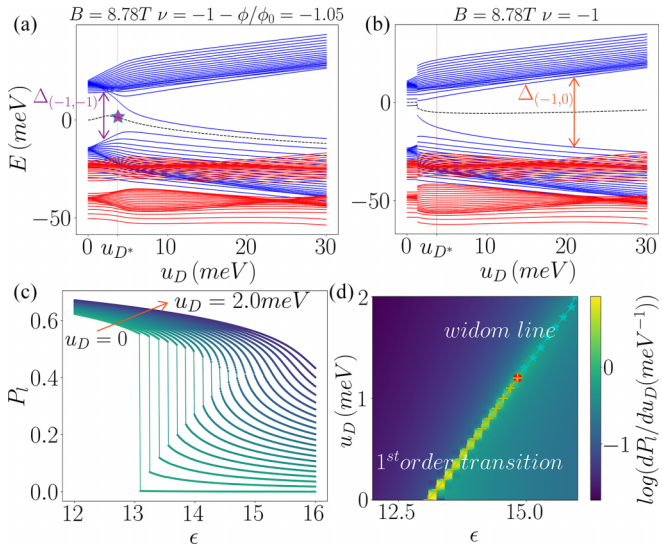

FIG. 3. (a) Hartree-Fock spectrum at $\epsilon = 20$ with varying u_D at $\nu = -1 - \frac{|\phi|}{\phi_0}$ and (b) $\nu = -1$. Topological phase transition at $B = 0$ is at u_{D^*}. (c), (d) Layer polarization P_l and polarizability with varying u_D and ϵ at $B = 8.78$ T.

Fig. 10 of Ref. [8]). Our calculation at $B \neq 0$ captures this effect. As shown in Fig. 3(a), at $\epsilon = 20$ chosen to recover the phenomenology of Ref. [8] at $B = 0$, we observe a crossover at D_* between a Chern paraelectric with a large gap and an ostensibly IQH state of a Landau quantized trivial insulator with one LL depopulated by electrons and a small gap. We refer to the latter as a QH ferroelectric because at $u_D = 0$ it breaks $C_{2y}\mathcal{T}$. Both states are spin polarized. The results of a separate Hartree-Fock calculation at $t = 0$ shown in Fig. 3(b) confirm the prominent trivial insulator with a large gap. Thus, the incompressible states can appear simultaneously at $\nu = -1$ and $\nu = -1 - \frac{|\phi|}{\phi_0}$ for a range of D near D_*.

In order to explore the robustness of the above results, as well as the tunability of the correlated phases, we perform the Hartree-Fock calculations at $s = -1$ and $t = -\mathrm{sgn}(B)$ at varying ϵ, u_D, and B. The resulting tentative phase diagram is shown in Fig. 2. At $D = 0$ the first-order topological transition at ϵ_* extends to $B \neq 0$ despite separating states with the same Chern number t at $B \neq 0$ because the QH ferroelectric on one side breaks $C_{2y}\mathcal{T}$ and the Chern paraelectric on the other does not. This first-order phase transition moves towards a stronger interaction as B increases, favoring the Chern paraelectric, i.e., the descendant of the QAH state. The transition must also extend to small nonzero D despite the explicit breaking of $C_{2y}\mathcal{T}$ by D because it starts out first order at $D = 0$. Indeed, Fig. 3(c) shows the jump in the layer polarization at a fixed B persisting to nonzero u_D, with D favoring the ferroelectric and the first-order transition terminating at a critical endpoint. As we show below, we can describe this using a simple Landau theory for an Ising ferroelectric with a negative quartic coupling. Upon varying B the critical endpoint extends to the red curve shown in Fig. 2. Interestingly, the D-induced crossover shown in Fig. 3(a) appears at B and ϵ notably separated from the critical endpoint. We understand it as crossing the Widom line, defined as the peak in the layer polarizability, extending beyond the critical endpoint as shown in Figs. 3(d) and 2.

As IVC is strongly suppressed by the B field, the Chern paraelectric and QH ferroelectric phases are the main phases in Fig. 2. Below we discuss our formalism and computational scheme that lead to the above results. We note in passing that at the twist angle 3.89°, $\phi = \phi_0$ at $B \simeq 176$ T, so to get below 9 T as in the experiments we need $\phi/\phi_0 \lesssim 1/20$. Reaching such a small flux efficiently in our interacting calculation is enabled by a recently developed technique [44–46] utilizing the $B = 0$ hybrid Wannier states to construct the basis at $B \neq 0$; some of our calculations go down to $\phi/\phi_0 = 1/47$.

Continuum model. The moiré bands of experimental relevance originate from the spin-valley locked valence bands of monolayer $MoTe_2$ [40]. The relations in Eqs. (1) and (2), as well as the stated experimental results, hold in any right-handed coordinate system (even though σ_{xy}, and therefore t, changes sign between two coordinate system choices related by a 180° rotation about the x or y axis). We are therefore free to choose any of the two out-of-plane directions as $\hat{\mathbf{z}}$ and we made the common choice [40] of aligning it with the spin angular momentum direction of the valley $\mathbf{K}$. Then, in valley $\mathbf{K}$ and for spin up, the noninteracting moiré band structure can be described by a continuum electronic model [3]:

$$H_{\mathbf{K}} = \int \mathrm{d}^2\mathbf{r}(\psi^\dagger_{b\mathbf{K}}(\mathbf{r})\psi^\dagger_{t\mathbf{K}}(\mathbf{r})) \times \begin{pmatrix} h_b(\mathbf{p}) + \Delta_b(\mathbf{r}) + \frac{u_D}{2} & \Delta_T(\mathbf{r}) \\ \Delta_T^*(\mathbf{r}) & h_t(\mathbf{p}) + \Delta_t(\mathbf{r}) - \frac{u_D}{2} \end{pmatrix} \times \begin{pmatrix} \psi_{b\mathbf{K}}(\mathbf{r}) \\ \psi_{t\mathbf{K}}(\mathbf{r}) \end{pmatrix}. \quad (3)$$

Here, $\psi^\dagger_{l\mathbf{K}}(\mathbf{r})$ creates an electron in layer $l = b, t$, in valley $\mathbf{K}$, and at position $\mathbf{r}$. $h_l(\mathbf{p}) = -(\mathbf{p} - \hbar\kappa_l)^2/2m^*$ is the kinetic energy, with $\mathbf{p} = -i\hbar\nabla_{\mathbf{r}}$ and effective mass m^*. κ_l points sit at the corners of the hexagonal moiré Brillouin zone, and we describe the effect of D by adding a potential difference u_D between two layers, where $\Delta_{b(t)}(\mathbf{r}) = 2V\sum_{j=1,3,5}\cos(\mathbf{G}_j \cdot \mathbf{r} \pm \phi)$ is the intralayer potential for the bottom (top) layer, and $\Delta_T(\mathbf{r}) = w(1 + e^{-i\mathbf{G}_2\cdot\mathbf{r}} + e^{-i\mathbf{G}_3\cdot\mathbf{r}})$ is the interlayer tunneling potential. The reciprocal lattice vector $\mathbf{G}_j$ is obtained by the counterclockwise rotation of $\mathbf{G}_1 = 4\pi/(\sqrt{3}a_M)\hat{\mathbf{x}}$ by angle $(j-1)\pi/3$. $a_M = a_0/\theta(\mathrm{rad})$ is the moiré superlattice constant, where a_0 is the lattice constant of monolayer $MoTe_2$. We choose parameters $(a_0, m^*, V, \phi, \omega) = (0.355\ \mathrm{nm}, 0.62m_e, 17.0\ \mathrm{meV}, +107.7°, -16.0\ \mathrm{meV})$ at twist angle $\theta = 3.89°$ [23]. The noninteracting model in the $\mathbf{K}'$ valley and for spin down is related by time reversal symmetry $\mathcal{T}$, which takes the complex conjugation of the 2×2 Hamiltonian in Eq. (3).

In an external magnetic field, we replace $\mathbf{p} \to \mathbf{p} + e\mathbf{A}$, where $\nabla \times \mathbf{A} = B\hat{\mathbf{z}}$, and add Zeeman coupling $\frac{1}{2}g\mu_B B\tau_0\sigma_z$, where τ_0 is the identity Pauli matrix acting on layer degrees of freedom, and σ_z is the spin Pauli matrix. At $B = 0$, the Hamiltonian is invariant under threefold out-of-plane rotation C_{3z}, in-plane twofold rotation symmetry about the y axis C_{2y}, and the time reversal symmetry $\mathcal{T}$. At this order the continuum Hamiltonian also has a pseudoinversion symmetry [19,47] $\mathcal{I}$ given by $\mathbf{r} \to -\mathbf{r}$ in each valley and flipping the layers with

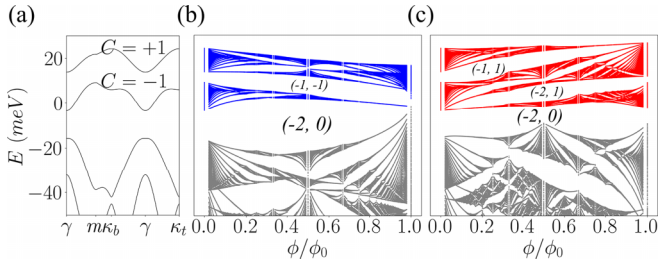

FIG. 4. (a) Band structure at $B = 0$ in the valley $\mathbf{K}$ for $tMoTe_2$ at $\theta = 3.89°$. (b), (c) Hofstader spectra at $\mathbf{K}$ and $\mathbf{K}'$, omitting Zeeman effect.

τ_1. While both C_{2y} and $\mathcal{T}$ are broken at $B \neq 0$, their product $C_{2y}\mathcal{T}$ is preserved, as are C_{3z} and $\mathcal{I}$. Figure 4(a) shows the noninteracting band structure at $B = 0$ in the valley $\mathbf{K}$ where the two uppermost bands carry Chern numbers $+1$ and -1. The band dispersion and Chern numbers in the opposite valley $\mathbf{K}'$ are related by $\mathcal{T}$. For $B > 0$ the corresponding Hofstadter spectra for the valleys $\mathbf{K}$ and $\mathbf{K}'$, together with the (s, t) labels of the gaps, are shown in Figs. 4(b) and 4(c), respectively. As can be seen by the evolution of the magnetic subbands, a Chern band gains or loses states per unit cell according to the relation $1 + t\phi/\phi_0$. To study the correlated phenomena, we project the Coulomb interaction onto the upper two Chern ± 1 bands of both valleys if at $B = 0$, i.e., two bands per valley, or the magnetic subbands emanating from these Chern bands if at $B \neq 0$,

$$H_V = \frac{e^2}{4\epsilon\epsilon_0 A} \sum_{\mathbf{q}\neq 0} \frac{1}{|\mathbf{q}|} \tanh(|\mathbf{q}|d) : \mathcal{P}\rho_{\mathbf{q}}\rho_{-\mathbf{q}}\mathcal{P} : . \quad (4)$$

Here, $\rho_{\mathbf{q}} = \sum_{\eta,l} \int d^2\mathbf{r} e^{-i\mathbf{q}\cdot\mathbf{r}} \psi^\dagger_{l\eta}(\mathbf{r})\psi_{l\eta}(\mathbf{r})$ is the Fourier transform of the electron density operator, with $\eta = \mathbf{K}$ or $\mathbf{K}'$, and total area A. In this work we consider a dual gate screened Coulomb interaction, d being the distance between each gate and $tMoTe_2$, taken to be 30 nm in our calculations, with the small distance between the two $MoTe_2$ layers neglected. The symbol :: denotes operator normal ordering with respect to the charge neutrality [19]. $\mathcal{P}$ projects onto the mentioned Hilbert subspace which can be generated at $B \neq 0$ by solving the noninteracting problem [29,44,45]. At the B values of interest here, expanding $\mathcal{P}$ in the LL basis proves to be computationally expensive when dealing with interactions. Instead, we construct the basis states using the $B = 0$ hybrid Wannier states method following Refs. [45,46].

Streda line near $\nu = -1$ and Zeeman effect. The $B > 0$ energy spectrum of candidate Chern states along the $(-1, \mp 1)$ lines is shown in Figs. 1(a)–1(d). We present their total energy per unit cell as a function of B at varying Zeeman g factors in Figs. 1(e)–1(h). The orbital contribution to the Zeeman effect stems from the d-orbital nature of the states in each valley [40]. The two-band $\mathbf{k}\cdot\mathbf{p}$ Hamiltonian describing the large semiconductor gap in $MoTe_2$ monolayer has the form of a massive $2+1$-dimensional $(2+1\text{D})$ Dirac Hamiltonian [40], whose minimal coupling to a low B field results in an additional $\frac{1}{2}\hbar\omega_c$ energy shift compared to a Schrödinger Hamiltonian. Since the Dirac mass effectively flips sign between different valleys, this orbital shift also flips sign; it adds to the usual spin Zeeman factor of 2 (see Supplemental Material [46] for details). Using the known effective mass of $MoTe_2$ we find it to be 3.23 and thus the total $g = 5.23$. Using the computed ground state energy of the QAH state at $B = 0$, we smoothly interpolate between the calculated energies at $B \neq 0$ and $B = 0$ at $g = 0$ using at most a second-order polynomial in B as shown by the dashed lines in Figs. 1(e) and 1(f). Because the Chern paraelectrics are fully valley polarized, their Zeeman energy can be obtained analytically. We can therefore find the critical B below which the valley switches for Chern paralectrics. As seen in Figs. 1(g) and 1(h) the crossing only occurs for the $(-1, 1)$ line. While at $g = 2$ it occurs at 5.01 T (cyan star), at the more realistic $g = 5.23$ it is $\sim$178 mT (red star). Thus any putative density-induced valley switching would occur in the regime where the effects of quenched disorder dominate in realistic devices [9,10], likely modifying the clean limit energetics obtained here.

Effects due to D field. The energy spectrum induced by the perpendicular electric field D at $\phi/\phi_0 = 1/20$, corresponding to $B = 8.78$ T, is shown in Fig. 3(a) along the $(-1, -1)$ line. The lowest unoccupied LL can be seen to detach from the unoccupied LL group as D increases and to closely approach the highest occupied LL. This is similar to the magnetic subband spectrum of an electron confined to move in a plane in a periodic potential and an out-of-plane uniform magnetic flux slightly smaller than ϕ_0 shown in Fig. 7 of Ref. [36] as the strength of the periodic potential increases and drives a transition from a Chern insulator (a broadened LL) and a trivial insulator at their $\phi = \phi_0$. As shown in Fig. 3(b) for $(-1, 0)$, a prominent trivial insulator is indeed stabilized in our Hartree-Fock calculation as well.

The evolution of the layer polarization $P_l = \frac{A_{uc}}{A}\sum_\eta \int d^2\mathbf{r}\langle\psi^\dagger_{b\eta}(\mathbf{r})\psi_{b\eta}(\mathbf{r}) - \psi^\dagger_{t\eta}(\mathbf{r})\psi_{t\eta}(\mathbf{r})\rangle$ and polarizability dP_l/du_D at $(-1, -1)$ with varying ϵ and D, at a fixed $B = 8.78$ T, are shown in Figs. 3(c) and 3(d). The main features can be captured by a simple Landau theory for an Ising order parameter, odd under $C_{2y}\mathcal{T}$,

$$\delta E = -\gamma u_D P_l + \frac{a(\epsilon)}{2}P_l^2 - \frac{b}{4}P_l^4 + \frac{1}{6}P_l^6. \quad (5)$$

Here, γ and b are positive constants, and the prefactor of P_l^6 was used to rescale the energy units. Decreasing a with decreasing ϵ causes the spontaneous symmetry breaking at $u_D \propto D = 0$ via a first-order phase transition due to the negative quartic term. At the critical endpoint, the local minima merge (see Supplemental Material [46]).

Phase diagram. The tentative three-dimensional (3D) phase diagram along the $(-1, -1)$ line is shown in Fig. 2. Markers correspond to parameters at which the transition, or a crossover in the case of Widom line, was calculated within Hartree-Fock. The solid lines and surfaces are interpolated based on physical arguments. At $u_D \propto D = 0$ the Chern paraelectric and the quantum Hall ferroelectric are distinguished by P_l, a Landau order parameter, and so must be separated by a phase transition. At $u_D \neq 0$, however, it is possible to transform one to another without encountering a phase transition by avoiding the (orange) surface of first-order phase transitions terminating in the (red) critical endpoint curve. The IVC is a sharply defined phase at any B and D because it breaks valley $U(1)$ symmetry, preserved by B and D while

the other phase(s) do not break it. It is suppressed by B even at $g = 0$, and further suppressed by the Zeeman effect. Therefore, while all the lines are computed at $g = 5.23$, the (cyan) phase boundary at $u_D = 16.8$ meV is extrapolated from the $g = 2$ markers; it moves closer to the $B = 0$ plane at higher g (see Supplemental Material [46]).

Discussion. Our calculation explains the presence of the $(-1, -1)$ line and the absence of the $(-1, +1)$ line in the experiments [7–10]. It also demonstrates the delicate balance between the energies of competing Chern states at $(-1, +1)$ polarized to opposite valleys, with the orbital Zeeman contribution ultimately deciding on the ground state with the small gap. Recent calculations [47–49] pointed out a rich evolution of the Chern bands and a lattice relaxation playing increasingly important role at low twist angles. While the Zeeman contribution is expected to be the same in the low-angle regime, the energetic differences due to the magnetic subbands shown in our Figs. 1(e) and 1(f) will change. It would be interesting to explore the possibility of density-induced switching of the Chern number at different angles or different homobilayers using the framework developed here.

Acknowledgments. We thank B. Andrei Bernevig, Fengcheng Wu, Di Xiao, Jian Kang, Eslam Khalaf, Jiabin Yu, Daniel Parker, Kin Fai Mak, Jie Shan, and Xiaodong Xu for helpful discussions. M.W. sincerely thanks Taige Wang for fruitful discussions and ongoing collaborations. X.W. acknowledges financial support from the National High Magnetic Field Laboratory through NSF Grant No. DMR-2128556 and the State of Florida. O.V. was funded by the Gordon and Betty Moore Foundation's EPiQS Initiative Grant No. GBMF11070. Part of the numerical computations were carried out on resources provided by the Planck clusters at Florida State University. M.W. acknowledge the Beijing Paratera Co., Ltd. for providing HPC resources that have contributed to the research results reported within this Letter.

[1] L. Balents, C. R. Dean, D. K. Efetov, and A. F. Young, Superconductivity and strong correlations in moiré flat bands, Nat. Phys. **16**, 725 (2020).

[2] D. M. Kennes, M. Claassen, L. Xian, A. Georges, A. J. Millis, J. Hone, C. R. Dean, D. Basov, A. N. Pasupathy, and A. Rubio, Moiré heterostructures as a condensed-matter quantum simulator, Nat. Phys. **17**, 155 (2021).

[3] F. Wu, T. Lovorn, E. Tutuc, I. Martin, and A. H. MacDonald, Topological insulators in twisted transition metal dichalcogenide homobilayers, Phys. Rev. Lett. **122**, 086402 (2019).

[4] T. Devakul, V. Crépel, Y. Zhang, and L. Fu, Magic in twisted transition metal dichalcogenide bilayers, Nat. Commun. **12**, 6730 (2021).

[5] T. Li, S. Jiang, B. Shen, Y. Zhang, L. Li, Z. Tao, T. Devakul, K. Watanabe, T. Taniguchi, L. Fu *et al.*, Quantum anomalous Hall effect from intertwined moiré bands, Nature (London) **600**, 641 (2021).

[6] Y.-M. Xie, C.-P. Zhang, J.-X. Hu, K. F. Mak, and K. T. Law, Valley-polarized quantum anomalous Hall state in moiré $MoTe_2/WSe_2$ heterobilayers, Phys. Rev. Lett. **128**, 026402 (2022).

[7] J. Cai, E. Anderson, C. Wang, X. Zhang, X. Liu, W. Holtzmann, Y. Zhang, F. Fan, T. Taniguchi, K. Watanabe *et al.*, Signatures of fractional quantum anomalous Hall states in twisted $MoTe_2$, Nature (London) **622**, 63 (2023).

[8] Y. Zeng, Z. Xia, K. Kang, J. Zhu, P. Knüppel, C. Vaswani, K. Watanabe, T. Taniguchi, K. F. Mak, and J. Shan, Thermodynamic evidence of fractional Chern insulator in moiré $MoTe_2$, Nature (London) **622**, 69 (2023).

[9] H. Park, J. Cai, E. Anderson, Y. Zhang, J. Zhu, X. Liu, C. Wang, W. Holtzmann, C. Hu, Z. Liu *et al.*, Observation of fractionally quantized anomalous Hall effect, Nature (London) **622**, 74 (2023).

[10] F. Xu, Z. Sun, T. Jia, C. Liu, C. Xu, C. Li, Y. Gu, K. Watanabe, T. Taniguchi, B. Tong *et al.*, Observation of integer and fractional quantum anomalous Hall effects in twisted bilayer $MoTe_2$, Phys. Rev. X **13**, 031037 (2023).

[11] T. Neupert, L. Santos, C. Chamon, and C. Mudry, Fractional quantum Hall states at zero magnetic field, Phys. Rev. Lett. **106**, 236804 (2011).

[12] D. Sheng, Z.-C. Gu, K. Sun, and L. Sheng, Fractional quantum Hall effect in the absence of Landau levels, Nat. Commun. **2**, 389 (2011).

[13] N. Regnault and B. A. Bernevig, Fractional Chern insulator, Phys. Rev. X **1**, 021014 (2011).

[14] E. Tang, J.-W. Mei, and X.-G. Wen, High-temperature fractional quantum Hall states, Phys. Rev. Lett. **106**, 236802 (2011).

[15] K. Sun, Z. Gu, H. Katsura, and S. Das Sarma, Nearly flatbands with nontrivial topology, Phys. Rev. Lett. **106**, 236803 (2011).

[16] A. Abouelkomsan, E. J. Bergholtz, and S. Chatterjee, Multiferroicity and topology in twisted transition metal dichalcogenides, Phys. Rev. Lett. **133**, 026801 (2024).

[17] C. Wang, X.-W. Zhang, X. Liu, Y. He, X. Xu, Y. Ran, T. Cao, and D. Xiao, Fractional Chern insulator in twisted bilayer $MoTe_2$, Phys. Rev. Lett. **132**, 036501 (2024).

[18] V. Crépel and L. Fu, Anomalous Hall metal and fractional Chern insulator in twisted transition metal dichalcogenides, Phys. Rev. B **107**, L201109 (2023).

[19] J. Yu, J. Herzog-Arbeitman, M. Wang, O. Vafek, B. A. Bernevig, and N. Regnault, Fractional Chern insulators versus nonmagnetic states in twisted bilayer $MoTe_2$, Phys. Rev. B **109**, 045147 (2024).

[20] H. Goldman, A. P. Reddy, N. Paul, and L. Fu, Zero-field composite Fermi liquid in twisted semiconductor bilayers, Phys. Rev. Lett. **131**, 136501 (2023).

[21] W.-X. Qiu, B. Li, X.-J. Luo, and F. Wu, Interaction-driven topological phase diagram of twisted bilayer $MoTe_2$, Phys. Rev. X **13**, 041026 (2023).

[22] T. Wang, T. Devakul, M. P. Zaletel, and L. Fu, Topological magnets and magnons in twisted bilayer $MoTe_2$ and WSe_2, arXiv:2306.02501.

[23] T. Wang, M. Wang, W. Kim, S. G. Louie, L. Fu, and M. P. Zaletel, Topology, magnetism and charge order in twisted $MoTe_2$ at higher integer hole fillings, arXiv:2312.12531.

[24] F.-R. Fan, C. Xiao, and W. Yao, Orbital Chern insulator at $\nu = -2$ in twisted $MoTe_2$, Phys. Rev. B **109**, L041403 (2024).
[25] X. Liu, Y. He, C. Wang, X.-W. Zhang, T. Cao, and D. Xiao, Gate-tunable antiferromagnetic Chern insulator in twisted bilayer transition metal dichalcogenides, Phys. Rev. Lett. **132**, 146401 (2024).
[26] X.-J. Luo, W.-X. Qiu, and F. Wu, Majorana zero modes in twisted transition metal dichalcogenide homobilayers, Phys. Rev. B **109**, L041103 (2024).
[27] B. Li, W.-X. Qiu, and F. Wu, Electrically tuned topology and magnetism in twisted bilayer $MoTe_2$ at $\nu_h = 1$, Phys. Rev. B **109**, L041106 (2024).
[28] X. Lu, B. Lian, G. Chaudhary, B. A. Piot, G. Romagnoli, K. Watanabe, T. Taniguchi, M. Poggio, A. H. MacDonald, B. A. Bernevig *et al.*, Multiple flat bands and topological Hofstadter butterfly in twisted bilayer graphene close to the second magic angle, Proc. Natl. Acad. Sci. USA **118**, e2100006118 (2021).
[29] B. A. Foutty, C. R. Kometter, T. Devakul, A. P. Reddy, K. Watanabe, T. Taniguchi, L. Fu, and B. E. Feldman, Mapping twist-tuned multiband topology in bilayer WSe_2, Science **384**, 343 (2024).
[30] P. Streda, Theory of quantised Hall conductivity in two dimensions, J. Phys. C: Solid State Phys. **15**, L717 (1982).
[31] A. Widom, Thermodynamic derivation of the Hall effect current, Phys. Lett. A **90**, 474 (1982).
[32] M. Kohmoto, Topological invariant and the quantization of the Hall conductance, Ann. Phys. **160**, 343 (1985).
[33] G. H. Wannier, A result not dependent on rationality for Bloch electrons in a magnetic field, Phys. Status Solidi B **88**, 757 (1978).
[34] D. J. Thouless, Quantization of particle transport, Phys. Rev. B **27**, 6083 (1983).
[35] A. H. MacDonald, Landau-level subband structure of electrons on a square lattice, Phys. Rev. B **28**, 6713 (1983).
[36] Z. Tešanović, F. Axel, and B. I. Halperin, "Hall" crystal versus Wigner crystal, Phys. Rev. B **39**, 8525 (1989).
[37] E. M. Spanton, A. A. Zibrov, H. Zhou, T. Taniguchi, K. Watanabe, M. P. Zaletel, and A. F. Young, Observation of fractional Chern insulators in a van der Waals heterostructure, Science **360**, 62 (2018).
[38] Y. Xie, A. T. Pierce, J. M. Park, D. E. Parker, E. Khalaf, P. Ledwith, Y. Cao, S. H. Lee, S. Chen, P. R. Forrester, K. Watanabe, T. Taniguchi, A. Vishwanath, P. Jarillo-Herrero, and A. Yacoby, Fractional Chern insulators in magic-angle twisted bilayer graphene, Nature (London) **600**, 439 (2021).
[39] X. Wang and O. Vafek, Theory of correlated Chern insulators in twisted bilayer graphene, Phys. Rev. X **14**, 021042 (2024).
[40] D. Xiao, G.-B. Liu, W. Feng, X. Xu, and W. Yao, Coupled spin and valley physics in monolayers of MoS_2 and other group-VI dichalcogenides, Phys. Rev. Lett. **108**, 196802 (2012).
[41] H. Pan, F. Wu, and S. Das Sarma, Band topology, Hubbard model, Heisenberg model, and Dzyaloshinskii-Moriya interaction in twisted bilayer WSe_2, Phys. Rev. Res. **2**, 033087 (2020).
[42] H. Polshyn, J. Zhu, M. A. Kumar, Y. Zhang, F. Yang, C. L. Tschirhart, M. Serlin, K. Watanabe, T. Taniguchi, A. H. MacDonald, and A. F. Young, Electrical switching of magnetic order in an orbital Chern insulator, Nature (London) **588**, 66 (2020).
[43] S. Zhang, H. Sheng, Z.-D. Song, C. Liang, Y. Jiang, S. Sun, Q. Wu, H. Weng, Z. Fang, X. Dai *et al.*, VASP2KP: $k \cdot p$ models and Landé g-factors from *ab initio* calculations, Chin. Phys. Lett. **40**, 127101 (2023).
[44] X. Wang and O. Vafek, Narrow bands in magnetic field and strong-coupling Hofstadter spectra, Phys. Rev. B **106**, L121111 (2022).
[45] X. Wang and O. Vafek, Revisiting Bloch electrons in a magnetic field: Hofstadter physics via hybrid Wannier states, Phys. Rev. B **108**, 245109 (2023).
[46] See Supplemental Material at http://link.aps.org/supplemental/10.1103/PhysRevB.110.L201107 for the orbital contribution to the g factor, Landau theory of the transition between Chern paraelectric and ferroelectric, as well as the hybrid Wannier basis at finite magnetic field.
[47] Y. Jia, J. Yu, J. Liu, J. Herzog-Arbeitman, Z. Qi, H. Pi, N. Regnault, H. Weng, B. A. Bernevig, and Q. Wu, Moiré fractional Chern insulators. I. First-principles calculations and continuum models of twisted bilayer $MoTe_2$, Phys. Rev. B **109**, 205121 (2024).
[48] X.-W. Zhang, C. Wang, X. Liu, Y. Fan, T. Cao, and D. Xiao, Polarization-driven band topology evolution in twisted $MoTe_2$ and WSe_2, Nat. Commun. **15**, 4223 (2024).
[49] N. Mao, C. Xu, J. Li, T. Bao, P. Liu, Y. Xu, C. Felser, L. Fu, and Y. Zhang, Transfer learning relaxation, electronic structure and continuum model for twisted bilayer $MoTe_2$, Commun. Phys. **7**, 262 (2024).